Wigner function based propagation of stochastic field emissions from planar electromagnetic sources

Gabriele Gradoni, *Member, IEEE,* Luk R. Arnaut, *Senior Member, IEEE,*
Stephen C. Creagh, Gregor Tanner, Mohd Hafiz Baharuddin, Christopher Smartt,
and David W. P. Thomas, *Senior Member, IEEE*

Abstract—Modelling the electromagnetic radiation from modern digital systems – acting effectively as extended, stochastic sources as part of a complex architecture – is a challenging task. We follow an approach here based on measuring and propagating field-field autocorrelation functions (ACFs) after suitable averaging. From the modelling side, we use the Wigner transform of the ACFs to describe random wave fields in terms of position and direction of propagation variables. An approximate propagator for the components of the radiated magnetic field is constructed for these ACFs based on a linear flow map. Field-field ACFs at aperture level are obtained from scanning measurements of complex sources. Distance and spatial resolution of the scanning plane is less than a wavelength from the source plane to capture the imprint of evanescent waves in the near-field ACFs. Near-field scanning and efficient near-to-far field propagation is carried out and compared with measurements. Results of this study will be useful to assist far-field predictions, source reconstruction, and emission source microscopy.

Index Terms—Statistical Electromagnetics, Near-field Scan, Wigner Function, Correlation, Reverberation Chamber.

I. INTRODUCTION

The emission of statistical electromagnetic sources, including printed circuit boards (PCBs) and integrated circuits (ICs), configures as a stochastic radiation pattern that has complex space-time behavior. The hallmarks of this class of sources are: having large spatial extent, fast and quasi-random time-domain transitions of inherent pin/track voltages, and low average power of the local radiated fields [1]. This constitutes a modelling challenge to be accounted for in existing and ongoing standardisation procedures [2]. Information about these sources can be obtained via Near-Field Scanning (NFS); the focus has been here in practice mainly on obtaining field emissions from time harmonic and deterministic sources [3], [4], [5]. Measuring the radiated emissions from PCBs has been used to study the electromagnetic fields in regions surrounding integrated circuits (ICs) [6], to estimate the currents flowing

G. Gradoni, S. C. Creagh, and G. Tanner are with the School of Mathematical Sciences, University of Nottingham, University Park, UK, e-mail: gabriele.gradoni@nottingham.ac.uk.

L. R. Arnaut is with the School of Electronic Engineering and Computer Science, Queen Mary University of London, Mile End Road, London E14FZ, U.K.

M. H. Baharuddin is with the George Green Institute for Electromagnetics Research, University of Nottingham, University Park, UK and Department of Electrical Electronic and Systems Engineering, Universiti Kebangsaan Malaysia, 43600 UKM Bangi, Selangor, Malaysia

C. Smartt, and D. W. P. Thomas are with the George Green Institute for Electromagnetics Research, University of Nottingham, University Park, UK.

through chips [7], and to extract effective dipole moments for source reconstruction [8], [9], [10], [11], [12], [13].

The aim of this work is to demonstrate that an approach introduced in [14] based on propagating ACFs from NFS measured field data using the so-called Wigner transformation is a viable alternative for stochastic field modelling. Near-to-Far Field (NFF) propagation is a delicate task as its computation, whether deterministic [15] or stochastic [16], [17], is computationally intensive. Efficient strategies have been proposed for deterministic sources using, e.g., the Boundary Element Method (BEM) [18], [19], [20], [21], and Fast Multipole Methods (FMM) [22], [18]. In [16] the ACF of the near field is expanded in eigenmodes through the Karhunen-Loève theorem, and each eigenvalue is propagated by using the canonical NFF transformations. A similar approach has been revisited and expanded in view of the Principal and Independent Component Analyses (PCA, ICA) for the field radiated by Ultra Wide Band (UWB) sources [23], [13], [24], [25]. In [26], the ACF approach has been used in source reconstruction and localisation.

In contrast to these approaches, we do not expand the (unknown) near-field ACF in a basis of modes. Rather, we apply a Wigner Function (WF) transformation to the ACF obtained from direct NFS measured fields: this gives a representation of waves in the combined space of their position and direction of propagation, or phase-space [27]. A NFF transformation for the ACF is derived as a linear map of functions on phase space, and compared against measured ACFs of a test statistical source at increasing distances away from the source. An aperture in a mode-stirred cavity is the test source of emitted stochastic fields. Synthetic aperture measurements on a plane close to the cavity backed aperture are used as input to the method. The proposed method allows for analysing the spatial ACF of a spatially continuous source or a set of discrete sources. The latter may be a wire array, for example, driven by voltages radiating partially correlated field components [14]. The knowledge of the ACF within planar surfaces at different distances from the source can be useful to assist source reconstruction methods [28], [29], [30], [31], far-field estimation [32], [33], as well as recently introduced phase-resolved scanning [34] and Emission Source Microscopy (ESM) methods [35]. Furthermore, the method can be used in conjunction with Huygens box method - also in its incomplete version when the radiation is suppressed through some box faces [33] - to augment the information on random field fluctuations. Alternative statistical methods have

been proposed in [23], [34]. Full two-probe measurements from PCBs can be propagated using the same approach upon appropriate space-time averaging. Preliminary experimental results indicating the non-stationary nature of massive memory transfer events in Galileo controller PCBs have been reported in [36].

The paper is organised as follows: in Section II, the WF based propagator is derived for ACFs. In Section III, the measurement set-up and the NFS procedure are explained together with an experimental validation of the theory. In Sec IV, we draw conclusions and offer future perspectives for the work.

II. THEORY

Consider an extended planar source radiating a noisy and quasi-random field. Field sampling is done at a spatial point $\mathbf{x} = (x, y)$ at time t in a plane parallel to the source and at a distance z from it. The measured field component is denoted

$$F(\mathbf{x}, z; t), \qquad t \in [0, T], \tag{1}$$

where T is the total observation time. We consider the field F in (1) to be a stochastic process subject to spatial fluctuations, assuming a time-harmonic $\exp(i\omega t)$ dependence.

A. Correlation and Wigner function

Starting from a stochastic radiated field, we define the correlation function of the fields sampled at two different spatial locations as

$$
\begin{aligned}
C_z(\mathbf{x}_a, \mathbf{x}_b; \tau) &= \langle F(\mathbf{x}_a, z; t + \tau) F(\mathbf{x}_b, z; t) \rangle \\
&= \lim_{T \to \infty} \frac{1}{T} \int_0^T F(\mathbf{x}_a, z; t + \tau) F(\mathbf{x}_b, z; t) \, dt,
\end{aligned}
\tag{2}
$$

where $\langle \cdot \rangle$ is an appropriate ensemble average. In the frequency domain, this field-field ACF is represented by

$$\Gamma_z(\mathbf{x}_a, \mathbf{x}_b; \omega) = \int_{-\infty}^{\infty} e^{-i\omega\tau} C_z(\mathbf{x}_a, \mathbf{x}_b; \tau) \, d\tau. \tag{3}$$

The averaging in (2) is performed on products of synchronised fields at two different points $\mathbf{x}_a$ and $\mathbf{x}_b$. It produces a function independent of the time reference in the case of stationary stochastic fields. For sources for which the signal is not controlled by the experiment, such as a PCB under operational conditions, a two-probe scanning system is used to measure the field at pairs of spatial positions simultaneously. Here, one probe is used to provide a stable phase reference [36], [30], [35]. As in applications for NFS for deterministic sources, a NFF transformation is required to propagate the ACF from statistical sources. The physical problem that we solve is the following: given the electromagnetic field measured in the near field at the incomplete Huygens surface at $z = 0$, we predict the field-field ACF at an arbitrary plane beyond the source $z > 0$. We start by noting that the propagated fields at the plane z can be predicted by the Stratton-Chu Boundary Integral Equation (BIE) or the dyadic second Green's identity [37], see Sec. II-B. The boundary-value problem can thus be solved by using the fields measured at $z = 0$ as boundary conditions. In the following, we show that this solution can be achieved

conveniently by changing from a position representation, $\mathbf{x}$, of the electric and magnetic field components to a momentum representation, defined in the frequency domain by

$$\tilde{F}(\mathbf{p}, z; \omega) = \int e^{-ik\mathbf{p}\cdot\mathbf{x}} F(\mathbf{x}, z; \omega) d\mathbf{x} \tag{4}$$

and by a corresponding double Fourier transform being used to define the ACF $\tilde{\Gamma}_z(\mathbf{p}_a, \mathbf{p}_b; \omega)$, with $\mathbf{p}_a$ and $\mathbf{p}_b$ respectively denoting the variables conjugate to $\mathbf{x}_a$ and $\mathbf{x}_b$. Integration in (4) is over a two-dimensional plane defined by fixing the coordinate z. In practical implementations, this integration is confined to the finite domain to be scanned, which is assumed to be large enough that the function $F(\mathbf{x}, z; \omega)$ is vanishingly small outside (see discussion in Sec. III-B). The momentum vector $\mathbf{p} = (p_x, p_y)$ has the geometrical meaning of the components of the wave vector parallel to the source plane, normalised so that

$$
\begin{aligned}
p_x &= \sin\theta\cos\phi, \tag{5} \\
p_y &= \sin\theta\sin\phi, \tag{6}
\end{aligned}
$$

and $|\mathbf{p}| = \sin\theta$ where θ is the angle of the ray with respect to the outward normal $\hat{z}$. ACFs of scalar fields radiated from arbitrary complex sources can be propagated efficiently in free-space through the WF approach [38], [14]. In this paper we extend the method to a tensorial setting appropriate to EM radiation. If the measurement is performed over $N \times N$ spatial points distributed within a scanning area, and for each field component of the EM field, the ACF can be naturally represented as a $3N \times 3N$ tensor $\underline{\Gamma}(\mathbf{x}_a, \mathbf{x}_b; \omega)$. We focus on one entry of this tensor. The WF has a direct connection with the ACF, and allows it to be expressed as a function on phase space, combining position and direction of the wave vector [14]. For a single component F of the EM field, we can define a scalar WF as

$$W_z(\mathbf{x}, \mathbf{p}) = \int e^{-ik\mathbf{p}\cdot\mathbf{s}} \Gamma_z(\mathbf{x}, \mathbf{s}) \, d\mathbf{s}, \tag{7}$$

where the function $\Gamma_z(\mathbf{x}, \mathbf{s})$ is obtained from (3) by a coordinate transformation

$$
\begin{aligned}
\mathbf{x} &= (\mathbf{x}_a + \mathbf{x}_b)/2, \\
\mathbf{s} &= \mathbf{x}_a - \mathbf{x}_b,
\end{aligned}
\tag{8}
$$

where $\mathbf{x}$ is the average position of a pair of field measurements, and $\mathbf{s}$ is the displacement between them. Note that from here we suppress dependence on frequency in notation for the ACF and its various transforms. The WF treats position and momentum variables symmetrically, and so (7) can be also attained from

$$W_z(\mathbf{x}, \mathbf{p}) = \left(\frac{k}{2\pi}\right)^2 \int e^{ik\mathbf{x}\cdot\mathbf{q}} \tilde{\Gamma}_z(\mathbf{p}, \mathbf{q}) \, d\mathbf{q}, \tag{9}$$

where $\tilde{\Gamma}_z(\mathbf{p}, \mathbf{q})$ is similarly obtained from $\tilde{\Gamma}_z(\mathbf{p}_a, \mathbf{p}_b; \omega)$ through the rotation

$$
\begin{aligned}
\mathbf{p} &= (\mathbf{p}_a + \mathbf{p}_b)/2, \\
\mathbf{q} &= \mathbf{p}_a - \mathbf{p}_b.
\end{aligned}
\tag{10}
$$

B. Solution of the boundary-value problem

The transverse electric and magnetic fields are denoted $\mathbf{E} = E_x\hat{x} + E_y\hat{y}$ and $\mathbf{H} = H_x\hat{x} + H_y\hat{y}$, respectively. In the notation of the previous section we may assign F to be one of the components $E_x, E_y, H_x,$ or H_y. These can be propagated to any plane parallel to $(x, y, z = 0)$ with the knowledge of the electric and magnetic fields at the boundary, $\mathbf{E}(x, y, z = 0)$ and $\mathbf{H}(x, y, z = 0)$, through the second dyadic Green identity [37]. One obtains for the electric field

$$\mathbf{E}(\mathbf{x}, z) = \int \left\{ [-i\omega\mu \, \hat{n} \times \mathbf{H}(\mathbf{x}', 0)] \cdot \underline{\underline{G}}_0(\mathbf{x}, \mathbf{x}', z) \right. \tag{11}$$
$$\left. + [\hat{n} \times \mathbf{E}(\mathbf{x}', 0)] \cdot \nabla \times \underline{\underline{G}}_0(\mathbf{x}, \mathbf{x}', z) \right\} d\mathbf{x}'$$

and for the magnetic field

$$\mathbf{H}(\mathbf{x}, z) = \int \left\{ \underline{\underline{G}}_0(\mathbf{x}, \mathbf{x}', z) \cdot [i\omega\epsilon \, \hat{n} \times \mathbf{E}(\mathbf{x}', 0)] \right. \tag{12}$$
$$\left. + \nabla \times \underline{\underline{G}}_0(\mathbf{x}, \mathbf{x}', z) \cdot [\hat{n} \times \mathbf{H}(\mathbf{x}', 0)] \right\} d\mathbf{x}',$$

where $\underline{\underline{G}}_0(\mathbf{x}, \mathbf{x}', z)$ denotes the free-space dyadic Green function from point $\mathbf{x}'$ on the plane $z = 0$ to point $\mathbf{x}$ on the plane labelled by $z > 0$.

A partial Fourier transform is performed to represent fields $\tilde{E}(\mathbf{p}, z)$ and $\tilde{H}(\mathbf{p}, z)$ in momentum representation according to the notation of (4). By exploiting translation invariance of Green's functions in free-space and using the convolution property of the Fourier transform, this operation converts (11) and (12) into algebraic equations

$$\tilde{\mathbf{E}}(\mathbf{p}, z) = \left[i\omega\mu\hat{n} \times \tilde{\mathbf{H}}(\mathbf{p}, 0) \right] \cdot \underline{\underline{\tilde{G}}}_0(\mathbf{p}, z) \tag{13}$$
$$- \left[\hat{n} \times \tilde{\mathbf{E}}(\mathbf{p}, 0) \right] \cdot \underline{\underline{\tilde{G}}}_1(\mathbf{p}, z) ,$$

for the electric field and

$$\tilde{\mathbf{H}}(\mathbf{p}, z) = i\omega\epsilon \, \underline{\underline{\tilde{G}}}_0(\mathbf{p}, z) \cdot \left[\hat{n} \times \tilde{\mathbf{E}}(\mathbf{p}, 0) \right] \tag{14}$$
$$- \underline{\underline{\tilde{G}}}_1(\mathbf{p}, z) \cdot \left[\hat{n} \times \tilde{\mathbf{H}}(\mathbf{p}, 0) \right]$$

for the magnetic field, where

$$\underline{\underline{\tilde{G}}}_0(\mathbf{p}, z) = \left(\underline{\underline{I}} - \mathbf{p}\mathbf{p} \right) \tilde{G}_0(\mathbf{p}, z) , \tag{15}$$

is the partial Fourier transform (to momentum space) of the free-space dyadic Green's function $\underline{\underline{G}}_0$ and

$$\underline{\underline{\tilde{G}}}_1(\mathbf{p}, z) = \left(ik\mathbf{p} \times \underline{\underline{I}} \right) \tilde{G}_0(\mathbf{p}, z) \tag{16}$$

is the partial Fourier transform of $\nabla \times \underline{\underline{G}}_0(\mathbf{x}, 0)$. Here,

$$\tilde{G}_0(\mathbf{p}, z) = \frac{e^{ikzT(\mathbf{p})}}{2ikT(\mathbf{p})} \tag{17}$$

denotes the Fourier representation of the 3D scalar free-space Green's function ([39], page 342) and

$$T(\mathbf{p}) = \left\{ \begin{array}{ll} \sqrt{1 - p^2} & \text{for } p^2 \leq 1 , \\ i\sqrt{p^2 - 1} & \text{for } p^2 > 1 \end{array} \right. \tag{18}$$

(with $p = |\mathbf{p}|$) represents the direction cosine of the wavevector normal to the source plane, extended so that it applies to evanescent ($p^2 > 1$) as well as propagating ($p^2 \leq 1$) waves.

C. Propagation of ACFs

We next proceed to deriving a propagation rule for ACFs in momentum space for individual Cartesian field components. Without loss of generality, we form the dot product of (13) and (14) with $\hat{x}$, and use the boundary surface impedance at $z = 0$ as described in the Appendix A. This yields a closed-form (plane-wave) field propagator

$$\tilde{E}_x(\mathbf{p}, z) = \tilde{E}_x(\mathbf{p}, 0) e^{ikzT(\mathbf{p})} , \tag{19}$$
$$\tilde{H}_x(\mathbf{p}, z) = \tilde{H}_x(\mathbf{p}, 0) e^{ikzT(\mathbf{p})} \tag{20}$$

and analogous propagation rules hold for $\tilde{E}_y(\mathbf{p}, z)$ and $\tilde{H}_y(\mathbf{p}, z)$.

Since the Cartesian field components propagate independently, one obtains the propagated ACF upon insertion of (19)-(20) in (2), with $\tilde{F} = \tilde{E}_x, \tilde{E}_y, \tilde{H}_x$ or $\tilde{H}_y$. Then

$$\tilde{\Gamma}_z(\mathbf{p}, \mathbf{q}) = e^{ikz[T(\mathbf{p}+\mathbf{q}/2) - T^*(\mathbf{p}-\mathbf{q}/2)]} \tilde{\Gamma}_0(\mathbf{p}, \mathbf{q}) , \tag{21}$$

using the notation of (10). The z components of the electric and magnetic fields normal to the source plane can be calculated from the transverse components. This can be seen explicitly by forming the dot product between (13) and (14) by $\hat{z}$, and using the boundary impedance obtained in the Appendix A for multiple transverse components.

For propagating the ACF from the source plane into the far-field it is advantageous to represent the ACF so that its positional and directional dependences are evident. This can be done through the WF transform. After inserting (21) into (9), we obtain

$$W_z(\mathbf{x}, \mathbf{p}) = \iint \mathcal{G}_z(\mathbf{x}, \mathbf{p}, \mathbf{x}', \mathbf{p}') W_0(\mathbf{x}', \mathbf{p}') \, d\mathbf{x}' \, d\mathbf{p}' \tag{22}$$

with a WF propagator given by

$$\mathcal{G}_z(\mathbf{x}, \mathbf{p}, \mathbf{x}', \mathbf{p}') = \left(\frac{k}{2\pi} \right)^2 \delta(\mathbf{p} - \mathbf{p}')$$
$$\int e^{ik(\mathbf{x}-\mathbf{x}')\cdot\mathbf{q} + ikz(T(\mathbf{p}+\mathbf{q}/2) - T^*(\mathbf{p}-\mathbf{q}/2))} \, d\mathbf{q} . \tag{23}$$

In [14], it is shown how the kernel $\mathcal{G}_z$ can be simplified through a ray-based approximation. The rationale of this approximation is that ACFs are smooth functions, and the spatial variation in the source correlation is assumed to take place on a scale that is larger than the wavelength. In this case, significant contributions to (23) are obtained at small values of $\mathbf{q}$ and approximate propagation is achieved by expanding $T(\mathbf{p}+\mathbf{q}/2)$ and $T^*(\mathbf{p}-\mathbf{q}/2)$ about $\mathbf{q} = \mathbf{0}$. Retaining only the leading order contribution, this yields a Dirac delta function

$$\mathcal{G}_z(\mathbf{x}, \mathbf{x}'; \mathbf{p}, \mathbf{p}') \approx \delta\left(\mathbf{x} - \mathbf{x}' - \frac{z\mathbf{p}}{T(\mathbf{p})} \right) \delta(\mathbf{p} - \mathbf{p}') \tag{24}$$

for propagating waves and

$$\mathcal{G}_z(\mathbf{x}, \mathbf{x}'; \mathbf{p}, \mathbf{p}') \approx e^{-2kz\sqrt{p^2-1}} \delta(\mathbf{p} - \mathbf{p}') , \tag{25}$$

for evanescent waves. Finally, using (24) and (25) in (22) reads

$$W_z(\mathbf{x}, \mathbf{p}) \approx \left\{ \begin{array}{l} W_0\left(\mathbf{x} - \frac{z\mathbf{p}}{T(\mathbf{p})}, \mathbf{p} \right) , \\ W_0(\mathbf{x}, \mathbf{p}) e^{-2kz\sqrt{p^2-1}} , \end{array} \right. \tag{26}$$
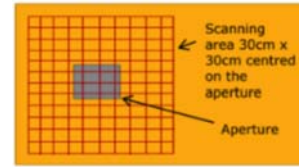
Fig. 1: A 3D scanner system.

Fig. 2: Scanning grid followed by the loop probe in the acquisition of field data. A subsampling raster of the actual grid is shown.

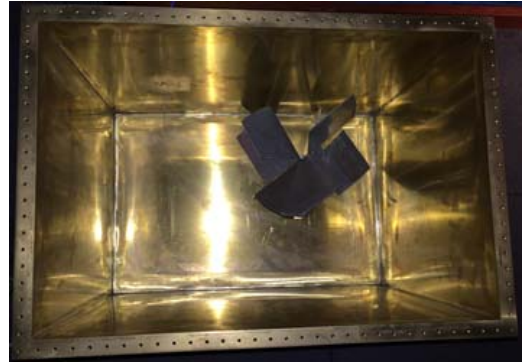Fig. 3: Box with the aperture panel removed to show the monopole antenna and rotating paddle.

thus leading to a ray-tracing approach for propagating waves and to a **p**-dependent damping rate for evanescent waves. This approximation of the transport rule for WFs in phase-space is obtained explicitly by retaining the leading order of the series expansion of the exponent of $\mathcal{G}_z$ in (22) [38], [14]. It is possible to go back to the ACF in configuration space by an inverse Fourier transform. Interestingly, $W_z\left(\mathbf{x}, \mathbf{p}\right)$ has the physical meaning of a (local) average radiation pattern of a statistical source. The propagation of the WF expressed in (26) results in a linear flow map in phase-space [38]. The flow takes a particular simple form in this approximation in free-space, propagating field intensities along straight lines with a tangent vector given by p from the source plane to the observation plane at z.

III. EXPERIMENTAL VALIDATION

For the validation of the approximate field-field correlation propagators in (26), a one-probe three-dimensional (3D) scanning system has been realised to perform measurements of a single field component radiated from the cavity backed aperture in Fig. 1. The experiment is done at a fixed frequency $f = 3$ GHz ($\lambda = 0.1$ m). The aperture has dimensions 8 cm × 8 cm. The cavity is a metallic rectangular enclosure of dimensions 1 m × 1 m × 0.5 m, with a mechanical mode stirrer in the interior. This structure is used to randomise the radiation from the monopole source inside the enclosure, forming a reverberation chamber (RC). In order to suppress background noise and external interferences in the measurement process, the whole scanner system has been put inside an anechoic chamber, as shown in Fig. 1.

A. Measurement set-up and parameters

The scanning rig performs measurements across a planar surface (synthetic aperture) adjacent to the cavity backed aperture as the device under test (DUT). A key component of this system is the antenna used to pick up the field radiated from the aperture, the Langer EMV-Technik RF R50-1 magnetic field probe shown in Fig. 1. This probe is a loop antenna of 1 cm diameter, with high magnetic field sensitivity and immunity to the electric field. The NFS is performed with sufficient spatial resolution, i.e., about 20 steps per wavelength, to accurately capture the far-field. A number of authors have studied the optimal choice of distance, spatial step, and width of the NFS plane. In particular, the distance and width of the scanning plane should be chosen so as to create a numerical aperture of 80° [40], and the spatial resolution should be half of the distance from the source [41]. This can be seen by rearranging Eq. (11) in [42] and assuming a dynamic range of 60 dB, resulting in an (in-plane) spatial step size $\Delta \approx \frac{z}{2}$ at a scan height $z \ll \lambda$. We performed the NFS in a plane at $z = 1$ cm from the aperture plane with a spatial step size of $\Delta = 0.5$ cm over an area of 0.3 m × 0.3 m, yielding $N = 60 \times 60 = 3600$ scan points per plane. However, measurements with larger spatial steps were also performed to assess the convergence of the results with respect to Δ. We have found that $\Delta = 0.5$ cm provides sufficient accuracy in a reasonable time. The scan raster grid is shown in Fig. 2. The DUT is depicted in Fig. 3 with the aperture plate removed to show the interior of the RC, the field mixing mechanical stirrer, and the wall mounted electric monopole antenna. Port 1 of the VNA was connected to the monopole; the field probe was connected to port 2. An Agilent E5062A vector network analyser (VNA) was used to measure the complex transmission parameter S_{21} and provides the phase reference. The NFS procedure is repeated at selected heights above the source plane. According to the van Cittert-Zernike theorem [43], [14], [23], it is expected that the correlation length increases, i.e., the field becomes more correlated, as the scanning plane moves away from the source plane. Specifically, at a distance $z \approx \lambda$
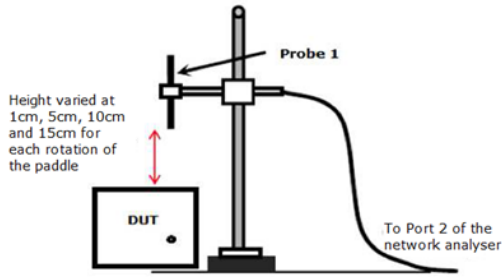
Fig. 4: Measurement set-up showing the scanning probe above the mode-stirred chamber: the radiation is randomized by the presence of the stirrer in the interior.
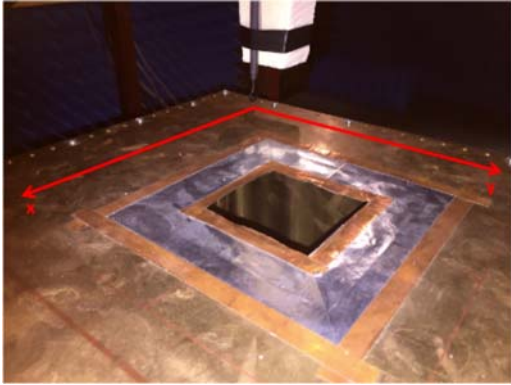

Fig. 5: Cavity with an aperture scan in progress.

the correlation length becomes of the order of the wavelength λ [44], [43], [14], [23].

B. Scanning process

The scanning process of N points per plane was carried out at $z = 1$ cm, 5 cm, 10 cm, and 15 cm above the source plane. The setup used is shown schematically in Fig. 4, while Fig. 5 shows the scanning process in progress. The S_{21} measurements are performed for 36 different paddle positions where the paddle position is increased by 10 degrees between each measurement. The field-field ACF is calculated from the ensemble average of the field data over all paddle positions, from (2), at every spatial point for each selected height z. For real sources, this correlation has a sensitive dependence on the separation between measurement points, while it varies slowly with the centre location of the measurement. Together with the increase in the correlation length, this can be used to reduce the number of measurements, as has been argued in [45], [31], [30]. However, this has not been done in our experiments.

From the 3D measurements, both the ACF and the WF follow, comprising of 4D data sets $\Gamma_z(x_1, y_1, x_2, y_2)$ and $W_z(x, y, p_x, p_y)$, respectively. These provide a challenge for visualisation of the data. As illustrated in Fig. 6, a 2D plot can be achieved by fixing a reference frame (x_1, y_1) for one field, and moving a scanning frame (x_2, y_2) for the other field considered in the calculation of the ACF. Figs. 7a, 7b and 7c show part of a 4D visualisation of the ACF and WF for scan
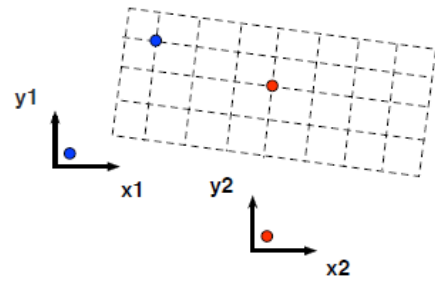

Fig. 6: 2D scanning grid containing sample fields. The ACF depends on 4 coordinates. A 2D plot can be achieved by fixing a reference frame (x_1, y_1), and moving a scanning frame (x_2, y_2).

heights at 1 cm; the ACF is obtained here from direct field measurements by ensemble averaging over 1, 16 and 36 stirrer positions, respectively. The corresponding WFs serve as input data W_0 for the propagator (26). For each measurement point and frequency we record S_{21} at 36 paddle positions. For each paddle position, the 3600 scanned locations across four planes give 14400 complex-valued data entries for S_{21}. Across all 36 paddle positions, this produces 518400 entries.

The data shown in Figs. 7a - 7c are obtained by taking the product between the field at the spatial points (x_2, y_2) and (x_1, y_1). The point (x_2, y_2) is fixed at the center of the scan, corresponding to $x_2 = y_2 = 0$, while the point (x_1, y_1) varies from $(-15, -15)$ cm to $(15, 15)$ cm with a step-size of 1 cm in the plot. The absolute value of the ACF is shown. The corresponding absolute value of the WF is located at $(y, p_y) = (0, 0)$ after Fourier transform of the displacement variables $x_1 - x_2$ and $y_1 - y_2$.

The subplots in Fig. 8 show again the absolute value of the WF as a function of x and p_x for fixed values of y and p_y, that is, $(y, p_y) = (0, 0)$, at $z = 1$ cm, 5cm, 10 cm, and 15 cm. The shearing of the WF for increasing z, as implied by (26) and described in [14], is clearly observed. The presence of multiple beams in the near-field WF in Fig. 8 is also interesting: these indicate local angular sectors where the average emission is particularly strong. This is important with a view towards defining emission patterns for statistical sources [23]. Finally, the presence of non-zero energy outside the interval $-1 \le p_x \le 1$ indicates the existence of complex angles of propagation associated with evanescent waves, as apparent from (26). The geometrical interpretation of WFs provides an intuitive way of capturing reactive near fields. In Fig. 8, the WF becomes concentrated within the area $-1 < p_x < +1$ as the transport coordinate z increases beyond $\lambda/2$, confirming that radiated energy is now carried by propagating (far-field) waves. Note that the finite transverse spatial range of measurement data taken further from the source truncates the ACF. Therefore the WF computed from this data misses detailed features that are expected from a simple propagation of the source data as represented by (26). Nevertheless the transformed data in Fig. 8 captures the shearing of phase space represented by the underlying free-space ray dynamics. We find good agreement (not shown) when the ACF propagated
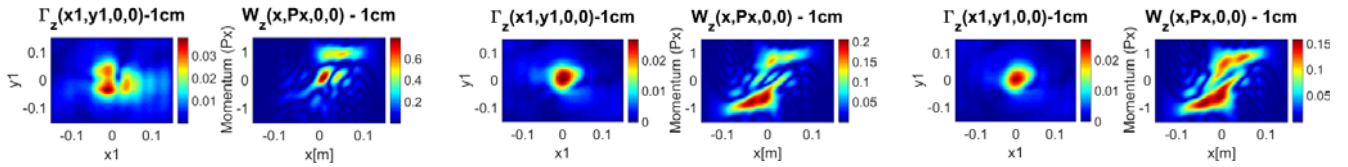
(a) Height $z = 1$ cm for one stirrer position. (b) Height $z = 1$ cm for 16 stirrer positions. (c) Height $z = 1$ cm for 36 stirrer positions.

Fig. 7: Plots show the absolute value of the field-field correlation function $\Gamma_z(x_1, y_1, x_2 = 0, y_2 = 0)$ (left panels) and the Wigner function $W_z(x, p_x, y = 0, p_y = 0)$ (right panels) at selected heights z above the source plane (where the centre of the aperture and scans is $(x, y) = 0$).
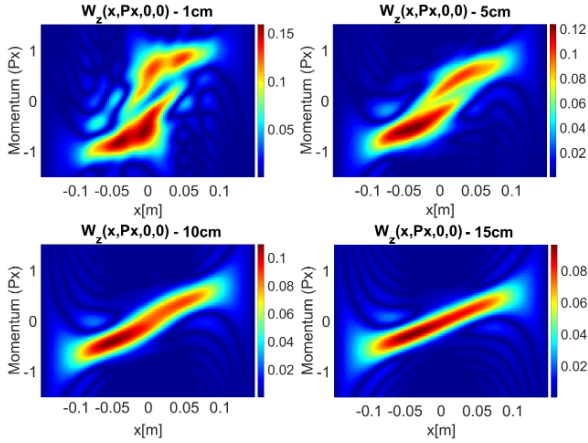

Fig. 8: Plots show the Wigner function at heights of 1 cm, 5 cm, 10 cm, and 15 cm (from top left to bottom right) obtained by averaging field data over an ensemble of 36 uncorrelated stirrer positions.

by (26) is truncated before evaluating the corresponding WF.

Fig. 9: ACF calculated from measured data (right plots) and from approximated propagators in (26) (left plots).

C. Theoretical and experimental comparison

The validation of the approximated NFF propagator is performed through a four-step procedure:

1) the experimental ACF is calculated (for an ensemble of 36 paddle positions) at 4 heights;
2) the WF transformation is performed for these 4 in-plane correlation data sets;
3) the theoretical WFs are estimated by propagating from the plane $z = 1$ cm to the 3 other (larger) heights using (26);
4) the inverse Wigner transformation of the propagated WF is calculated to estimate the predicted ACFs at the 4 heights.

The near field WF at $z = 1$ cm in Fig. 7c acts as the initial WF (note that here $W_0 = W_{z=1\text{ cm}}$) to be propagated to $z = 5$ cm, 10 cm, and 15 cm through (26). A comparison between the propagated ACF and the ACF obtained from direct measurement is reported in Fig. 9 for the 4 scanning planes. The ACF is seen to be localized, as it represents the correlation of one grid point with all the other grid points; the correlation width increases linearly with z, as expected and in qualitative agreement with Fig. 3 in [23]; its maximum
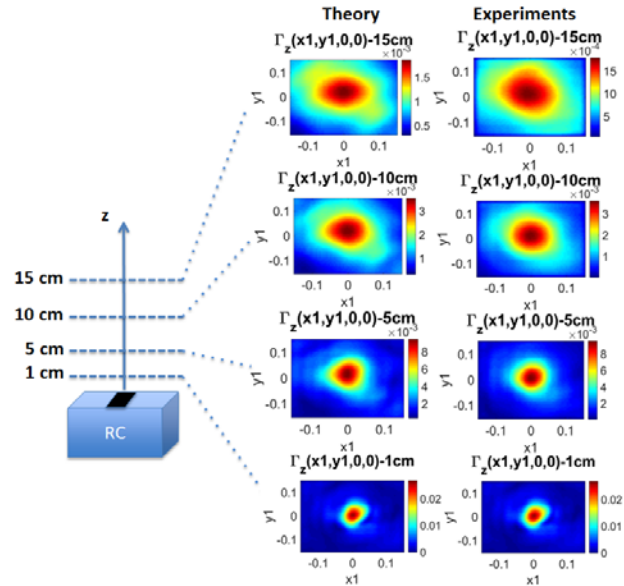
value scales by a factor of about 10 for each investigated plane. These three features are predicted accurately by the approximate propagators.

A sub-range of the full 4D ACF can be visualised using a mosaic-like plot (see Fig. 6), in which each individual tile of the mosaic shows $\Gamma_z(x_1, y_1, x_2, y_2)$ a fixed value of (x_2, y_2), while (x_1, y_1) varies over the whole scan. Moving from tile to tile in the x (or y) direction changes the value of x_2 (or y_2), by one measurement step of the probe, or 0.5 cm. To be specific, we show 4×4 subplots for both measured and propagated correlations at the three scanned heights in Figs. 10, 11, and 12, in which x_2 and y_2 defining individual tiles vary between probe positions numbered 28 to 31 (out of a total of 60 measurements in each dimension). These plots demonstrate that 4D ACFs can be propagated efficiently by using (26). As a distinctive feature of the correlation behaviour in the aperture, we notice that collective spreading - increase of the correlation length - and peak scaling from the upper left corner toward the lower right corner are tracked faithfully by the theoretical predictions.

A better way of comparing measurements and predictions can be obtained by projecting the WF onto the position

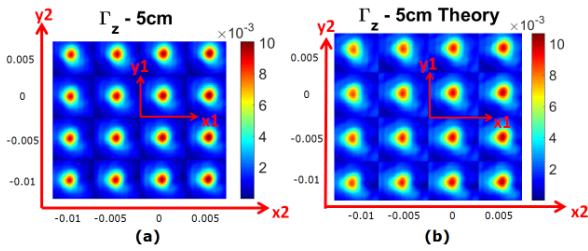

Fig. 10: 4D visualisation of measured (a) versus propagated (b) ACF at $z = 5$ cm.
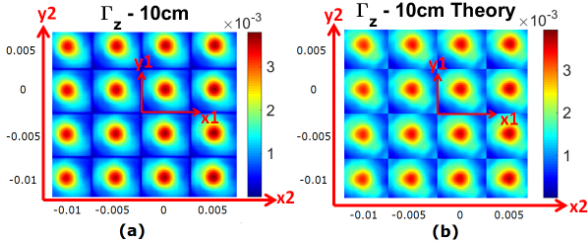

Fig. 11: 4D visualisation of measured (a) versus propagated (b) ACF at $z = 10$ cm.

coordinates $\mathbf{x}$. This gives the local field intensity of the random emission, and reduces the 4D representation to a 2D plot

$$\mathcal{I}(\mathbf{x}) = \frac{k}{2\pi} \iint W_z(\mathbf{x}, \mathbf{p}) \ d\mathbf{p} = \Gamma(\mathbf{x}, \mathbf{x}). \qquad (27)$$

The comparison between propagated and measured intensities in Figs. 13a, 13b and 13c shows good agreement. The discrepancies observed in the prediction of the average intensity are more pronounced at distances $z \geq \lambda$. They can be ascribed to several artefacts of the measurement process, including reduction of the signal-to-noise ratio of the field probe at large distances from the source; absence of probe correction; noise and EMI of the amplifier; other components in the measurements layout. Whilst we have made our best efforts at minimising the errors in the measurement process, potential sources of discrepancy in the measurement are scattering from the environment, including the scanner and the absorbers. The measurement is somewhat invasive in that the local field will be perturbed as the probe moves from one probe location to another during the scan. Furthermore, since the source plane is finite, diffraction by edges of the aperture will scatter fields towards the scanning region.
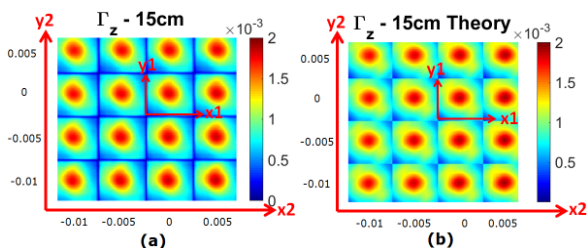

Fig. 12: 4D visualisation of measured (a) versus propagated (b) ACF at $z = 15$ cm.

IV. CONCLUSION

In this paper, a near-to-far field propagator for ACFs has been derived based on a Wigner function representation. The Wigner function propagator is independent of a modal expansion of radiated fields and extracts both positional and directional information from the correlation as well as evanescent (deep near-field) waves contributions. A proof-of-principle experiment as a validation of this approach is presented for a single magnetic field component radiated from a cavity backed aperture, the cavity being a reverberation chamber with monopole antenna. The cavity backed aperture has been adopted as a model statistical source, as it is able to produce a complex radiation pattern that changes in both space and time. Synthetic aperture measurements have been performed at different planes away from the aperture plane; the spatial ACF has been derived from field data and compared with the theory. Practical considerations on distance and resolution of the scanning procedure have been made in connection with the presence of sub wavelength detail, whose sampling is important to predict far-field radiation accurately. Results are useful to extend current near-to-far field methodologies, to perform source reconstruction of arbitrary devices, and to improve holographic source reconstruction methods, e.g., emission source microscopy.

APPENDIX

To solve the dyadic BIE and to obtain the field propagator in momentum space, i.e., in the space of the direction of the wave vector for E_x, we dot (13) by $\hat{x}$ to get

$$\begin{aligned} \tilde{E}_x(\mathbf{p}, z) = -i\omega\mu\Big[& p_x p_y \tilde{H}_x(\mathbf{p}, 0) \\ & + (1 - p_x^2) \tilde{H}_y(\mathbf{p}, 0) \Big] \tilde{G}_0(\mathbf{p}, z) \quad (28) \\ & + \Big(ikT(\mathbf{p}) \tilde{E}_x(\mathbf{p}, 0) \Big) \tilde{G}_0(\mathbf{p}, z). \end{aligned}$$

With (17), the dyadic boundary surface impedance at $z = 0$ is specified by

$$\tilde{E}_x(\mathbf{p}, 0) = -\eta_0 \left[\left(\frac{1 - p_x^2}{T(\mathbf{p})} \right) \tilde{H}_y(\mathbf{p}, 0) + \left(\frac{p_x p_y}{T(\mathbf{p})} \right) \tilde{H}_x(\mathbf{p}, 0) \right]. \quad (29)$$

Using (29) to eliminate $\tilde{H}_x$ and $\tilde{H}_y$ in (28), this yields the propagator (19). Similar surface impedance conditions can be derived *mutatis mutandis* for the other fields components.

REFERENCES

[1] M. I. Montrose, *EMC and the Printed Circuit Board: Design, Theory, and Layout Made Simple*. New York: IEEE Press., 2004.

[2] A. Ramanujan, F. Lafon, and P. Fernandez-Lopez, "Radiated emissions modelling from near-field data - toward international standards," in *Proc. 2015 Asia-Pacific International Symposium on Electromagnetic Compatibility (APEMC)*, Taipei, Taiwan, May 2015, pp. 90–93.
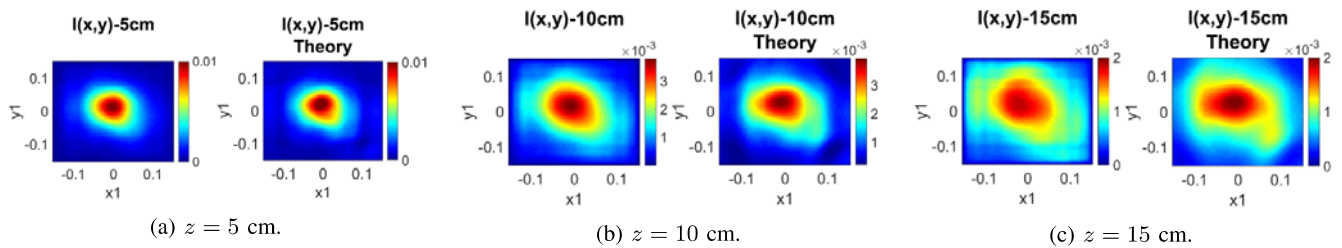
(a) $z = 5$ cm. (b) $z = 10$ cm. (c) $z = 15$ cm.

Fig. 13: 2D intensity $\mathcal{I}(x,y)$ plots at selected heights away from the source: ACF from measured data (a) vs WF approximation calculation (b).

[3] A. D. Yaghjian, "An overview of near-field antenna measurements," *IEEE Trans. Antennas Propag.*, vol. 34, pp. 30–45, Jan. 1986.

[4] J. E. Hansen, *Spherical Near-field Antenna Measurements*. London: Peregrinus, 1988.

[5] J. Fan, "Near-field scanning for EM emission characterization," *IEEE Electromagn. Compat. Mag.*, vol. 4, no. 3, pp. 67–73, 2015.

[6] G. Y. Cho and W. S. Park, "On the validity of approximate formulas for correlating TEM cell and near-field transmission measurement," *IEEE Trans. Electromagn. Compat.*, vol. 57, no. 2, pp. 173–179, Apr. 2015.

[7] Z. Yu, J. A. Mix, S. Sajuyigbe, K. P. Slattery, and J. Fan, "An improved dipole-moment model based on near-field scanning for characterizing near-field coupling and far-field radiation from an IC," *IEEE Trans. Electromagn. Compat.*, vol. 55, no. 1, pp. 97–108, Feb. 2013.

[8] Y. Vives-Gilabert, C. Arcambal, A. Louis, F. de Daran, P. Eudeline, and B. Mazari, "Modeling magnetic radiations of electronic circuits using near-field scanning method," *IEEE Trans. Electromagn. Compat.*, vol. 49, no. 2, pp. 391–400, May 2007.

[9] P. Fernandez-Lopez, C. Arcambal, D. Baudry, S. Verdeyme, and B. Mazari, "Simple electromagnetic modeling procedure: From near-field measurements to commercial electromagnetic simulation tool," *IEEE Trans. Instrum. Meas.*, vol. 59, no. 12, pp. 3111–3121, Dec. 2010.

[10] X. Tong, D. W. P. Thomas, A. Nothofer, P. Sewell, and C. Christopoulos, "Modeling electromagnetic emissions from printed circuit boards in closed environments using equivalent dipoles," *IEEE Trans. Electromagn. Compat.*, vol. 52, no. 2, pp. 462–470, May 2010.

[11] ——, "Reduction of sensitivity to measurement errors in the derivation of equivalent models of emission in numerical computation," in *Proc. IET 8th International Conference on Computation in Electromagnetics (CEM 2011)*, Wroclaw, Poland, Apr. 2011, pp. 1–2.

[12] H. Shall, Z. Riah, and M. Kadi, "A novel approach for modeling near-field coupling with PCB traces," *IEEE Trans. Electromagn. Compat.*, vol. 56, no. 5, pp. 1194–1201, Oct. 2014.

[13] L. R. Arnaut, C. S. Obiekezie, and D. W. P. Thomas, "Empirical emission eigenmodes of printed circuit boards," *IEEE Trans. Electromagn. Compat.*, vol. 56, no. 3, pp. 715–725, Jun. 2014.

[14] G. Gradoni, S. C. Creagh, G. Tanner, C. Smartt, and D. W. P. Thomas, "A phase-space approach for propagating field-field correlation functions," *New Journal of Physics*, vol. 17, no. 9, p. 093027, Sep. 2015.

[15] T. K. Sarkar and A. Taaghol, "Near-field to near/far-field transformation for arbitrary near-field geometry utilizing an equivalent electric current and MoM," *IEEE Trans. Antennas Propag.*, vol. 47, no. 3, pp. 566–573, Mar. 1999.

[16] B. Fourestie, Z. Altman, J.-C. Bolomey, J. Wiart, and F. Brouaye, "Statistical modal analysis applied to near-field measurements of random emissions," *IEEE Trans. Antennas Propag.*, vol. 50, no. 12, pp. 1803–1812, Dec. 2002.

[17] B. Fourestie, J.-C. Bolomey, T. Sarrebourse, Z. Altman, and J. Wiart, "Spherical near field facility for characterizing random emissions," *IEEE Trans. Antennas Propag.*, vol. 53, no. 8, pp. 2582–2589, Aug. 2005.

[18] C. Schmidt, M. Leibfritz, and T. Eibert, "Fully probe-corrected near-field far-field transformation employing plane wave expansion and diagonal translation operators," *IEEE Trans. Antennas Propag.*, vol. 56, no. 3, pp. 737–746, Mar. 2008.

[19] J. Quijano and G. Vecchi, "Field and source equivalence in source reconstruction on 3D surfaces," *Progress In Electromagnetics Research*, vol. 103, pp. 67–100, 2010.

[20] M. Borsero, O. Bottauscio, L. Zilberti, M. Chiampi, and W. Wang, "A boundary element estimate of radiated emissions produced by unknown sources," in *Proc. 2012 International Symposium on Electromagnetic Compatibility (EMC EUROPE)*, Rome, Italy, Sep. 2012, pp. 1–6.

[21] W. Wencui, O. Bottauscio, M. Chiampi, D. Giordano, and L. Zilberti, "An experimental-computational technique for evaluating magnetic field distributions around unknown sources," *IEEE Trans. Magn.*, vol. 49, no. 3, pp. 1143–1148, Mar. 2013.

[22] A. Tzoulis and T. Eibert, "Efficient electromagnetic near-field computation by the multilevel fast multipole method employing mixed near-field/far-field translations," *IEEE Antennas Wireless Propag. Lett.*, vol. 4, no. 1, pp. 449–452, Dec. 2005.

[23] L. R. Arnaut and C. S. Obiekezie, "Stochastic analysis of wideband near-field emissions from dipole antennas and integrated circuits," *IEEE Trans. Electromagn. Compat.*, vol. 56, no. 1, pp. 93–101, Feb. 2014.

[24] ——, "Source separation for wideband energy emissions using complex independent component analysis," *IEEE Trans. Electromagn. Compat.*, vol. 56, no. 3, pp. 559–570, Jun. 2014.

[25] ——, "Comparison of complex principal and independent components for quasi-gaussian radiated emissions from printed circuit boards," *IEEE Trans. Electromagn. Compat.*, vol. 56, no. 6, pp. 1598–1603, Dec. 2014.

[26] B. Nishina and Q. Chen, "Estimation of equivalent current distribution of modulated em radiation source," *IEEE Trans. Antennas Propag.*, vol. 64, no. 4, pp. 1334–1341, Apr. 2016.

[27] N. Marcuvitz, "The quasiparticle view of wave propagation," *Proceeding of the IEEE*, vol. 79, no. 10, pp. 1350–1358, Oct. 1991.

[28] A. Capozzoli, C. Curcio, A. Liseno, and P. Vinetti, "Field sampling and field reconstruction: A new perspective," *Radio Science*, vol. 45, no. 6, 2010.

[29] A. Gorbunova, A. Baev, M. Konovalyuk, Y. Kuznetsov, and J. Russer, "Stochastic EMI sources localization algorithm based on time domain planar near-field scanning," in *Proc. 2013 International Symposium on Electromagnetic Compatibility (EMC EUROPE)*, Wroclaw, Poland, Sep. 2013, pp. 972–976.

[30] J. A. Russer and P. Russer, "Modeling of noisy em field propagation using correlation information," *IEEE Trans. Microw. Theory Tech.*, vol. 63, no. 1, pp. 76–89, Jan. 2015.

[31] J. Russer, G. Gradoni, G. Tanner, S. Creagh, D. Thomas, C. Smartt, and P. Russer, "Evolution of transverse correlation in stochastic electromagnetic fields," in *Proc. 2015 International Microwave Symposium (IEEE MTT-S)*, Phoenix, AZ, May 2015, pp. 1–3.

[32] H. Weng, D. G. Beetner, and R. E. DuBroff, "Prediction of radiated emissions using near-field measurements," *IEEE Trans. Electromagn. Compat.*, vol. 53, no. 4, pp. 891–899, Nov. 2011.

[33] X. Gao, J. Fan, Z. Yaojiang, H. Kajbaf, and D. Pommerenke, "Far-field prediction using only magnetic near-field scanning for EMI test," *IEEE Trans. Electromagn. Compat.*, vol. 56, no. 6, pp. 1335–1343, Dec. 2014.

[34] T. Li, V. Khilkevich, and D. Pommerenke, "Phase-resolved near-field scan over random fields," *IEEE Trans. Electromagn. Compat.*, vol. 58, no. 2, pp. 506–511, Apr. 2016.

[35] P. Maheshwari, H. Kajbaf, V. V. Khilkevich, and D. Pommerenke, "Emission source microscopy technique for EMI source localization," *IEEE Trans. Electromagn. Compat.*, vol. 58, no. 3, pp. 729–737, Jun. 2016.

[36] C. Smartt, D. Thomas, H. Nasser, M. Baharuddin, G. Gradoni, S. Creagh, and G. Tanner, "Challenges of time domain measurement of field-field correlation for complex PCBs," in *Proc. 2015 IEEE International Symposium on Electromagnetic Compatibility (EMC EUROPE)*, Dresden, Germany, Aug. 2015, pp. 953–958.

[37] C. T. Tai, *Dyadic Green Functions in Electromagnetic Theory*. New York: IEEE Press., 1996.

[38] G. Gradoni, S. Creagh, and G. Tanner, "A Wigner function approach for describing the radiation of complex sources," in *Proc. 2014 IEEE Inter-

national Symposium on Electromagnetic Compatibility (EMC), Raleigh, NC, Aug. 2014, pp. 882–887.

[39] G. Barton, *Elements of Green's Functions and Propagation: Potentials, Diffusion, and Waves*. Oxford: Clarendon Press., 1989.

[40] X. Ren, P. Maheshwari, Y. j. Zhang, V. Khilkevich, J. Fan, Y. Zhou, Y. Bai, and X. Yu, "The impact of near-field scanning size on the accuracy of far-field estimation," in *Proc. 2014 IEEE International Symposium on Electromagnetic Compatibility (EMC)*, Raleigh, NC, Aug. 2014, pp. 582–587.

[41] D. Thomas, C. Obiekezie, S. Greedy, A. Nothofer, and P. Sewell, "Characterisation of noisy electromagnetic fields from circuits using the correlation of equivalent sources," in *Proc. 2012 International Symposium on Electromagnetic Compatibility (EMC EUROPE)*, Rome, Italy, Aug. 2012, pp. 1–5.

[42] E. Joy and D. Paris, "Spatial sampling and filtering in near-field measurements," *IEEE Trans. Antennas Propag.*, vol. 20, no. 3, pp. 253–261, May 1972.

[43] R. Cerbino, "Correlations of light in the deep Fresnel region: An extended Van Cittert and Zernike theorem," *Phys. Rev. A*, vol. 75, no. 5, p. 053815, May 2007.

[44] M. Born and E. Wolf, *Principles of Optics: Electromagnetic Theory of Propagation, Interference and Diffraction of Light*. Cambridge: Cambridge University Press., 2000.

[45] A. Baev, A. Gorbunova, M. Konovalyuk, Y. Kuznetsov, and J. Russer, "Stochastic EMI sources localization based on ultra wide band near-field measurements," in *Proc. European Microwave Conference (EuMC)*, Nuremberg, Germany, Oct. 2013, pp. 1131–1134.